Decentralized Interleaving of Parallel-connected Buck Converters

Mohit Sinha, *Student Member, IEEE*, Jason Poon, *Student Member, IEEE*, Brian B. Johnson, *Member, IEEE*, Miguel Rodriguez, *Member, IEEE*, and Sairaj V. Dhople, *Member, IEEE*

***Abstract*—We present a decentralized control strategy that yields switch interleaving for parallel-connected dc–dc buck converters. Compared to state-of-the-art methods that are distributed at best, the proposed architecture requires no communication, and hence, presents a variety of advantages with regard to reliability, modularity, and cost. The method is based on the digital implementation of the dynamics of a Liénard-type oscillator circuit as the controller for the converters. Each controller only requires the locally measured output current to synthesize the pulsewidth modulation (PWM) carrier waveform. The intrinsic electrical coupling between converters drives the nonlinear-oscillator-based controllers to converge to an interleaved state with uniform phase spacing across PWM carriers, independent of the number of converters, the load, and initial conditions. We provide analytical guarantees for existence and stability of the interleaved state as well as extensive hardware results for a system of five 120 W 48 V-to-12 V dc–dc buck converters that demonstrate convergence to the interleaved state in the face of a variety of large-signal disturbances.**

***Index Terms*—Decentralized control, multiphase converters, nonlinear control, switch interleaving.**

I. Introduction

THIS paper presents a decentralized switch-interleaving control strategy for multiphase dc–dc buck converters serving a common load. The architecture presents no single point of failure and requires no communication between the converters. The proposed controller is grounded on the dynamics of a type of nonlinear oscillator engineered such that the interleaved state is characterized by the minimum stored energy in a collection of such nonlinear oscillators. Convergence

Manuscript received May 4, 2018; revised July 22, 2018; accepted August 20, 2018. Date of publication September 3, 2018; date of current version March 29, 2019. This work was supported in part by the U.S. Department of Energy Solar Energy Technologies Office under Contract DE-EE0000-1583 and in part by the National Science Foundation under Grant ECCS-1509277. Recommended for publication by Associate Editor W. Huang. *(Corresponding author: Sairaj V. Dhople.)*

M. Sinha and S. V. Dhople are with the Department of Electrical and Computer Engineering, University of Minnesota, Minneapolis, MN 55455 USA (e-mail:

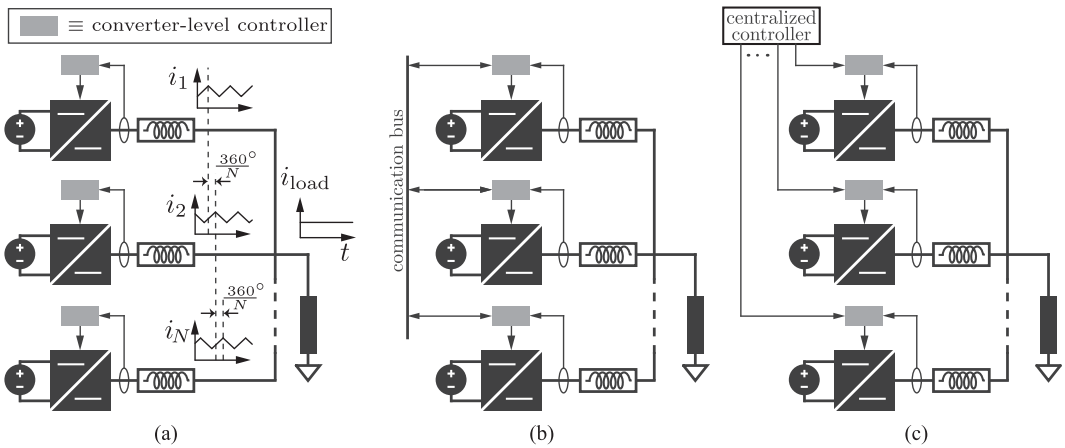

Fig. 1. Proposed approach to interleaving is (a) decentralized, representing a paradigm shift since it is communication free with no single point of failure. State-of-the-art methods for interleaving are (b) distributed, requiring a communication bus [1], [2]. Majority of the literature on interleaving focuses on switch timing managed (c) centrally [3]–[8]. (Current waveforms not shown in (b) and (c) for conciseness.) (a) Decentralized. (b) Distributed. (c) Centralized.

for each converter acts as an input to the oscillator, and the oscillator dynamical states are used to generate the corresponding triangular pulsewidth modulation (PWM) carrier (see Fig. 2 for details). Liénard oscillator dynamics have been examined in a variety of scientific and engineering disciplines [16]. Tangentially related to the application at hand, they have been used to realize decentralized real-time synchronization of ac voltages for inverters in microgrids [17]–[21], adaptive synchronization of grid-connected three-phase inverters [22], and carrier wave synchronization for three-phase parallel-connected inverters to suppress circulating currents [23]. While these studies examined *synchronization* of waveforms in the context of *ac* systems, here, we focus on the dual problem of *interleaving* PWM waveforms for *dc* systems. Theoretical foundations for this work are grounded on passivity-based frameworks to examine the networked dynamics of nonlinear oscillators. This is an expansive research topic; see, e.g., [24]–[28].

The theoretical and experimental results in this paper are presented with buck converters serving as the topology of choice in the parallel-connected multiphase system. However, it must be noted that the analytical approach and the feedback-synthesis method developed here can conceivably be applied to other converter topologies and network architectures. Focusing on the application at hand, while the proposed nonlinear controllers generate the interleaved PWM carriers, we leverage outer-loop droop controllers to ensure decentralized proportional power sharing [3]. From a theoretical vantage point, the main contribution of this paper is to establish analytical guarantees for the existence and stability of the interleaved solutions. To that end, we build a model for the parallel-connected converter system based on the collective dynamics of the oscillators, buck converters, and the electrical network. Then, we leverage a coordinate transformation of the system dynamics to polar coordinates to extract amplitude and phase information of the PWM waveforms. Following this, we enumerate and discuss the stability of equilibria that result from the involved dynamics.

This paper builds on our preliminary work in [29], where a similar feedback strategy was validated with numerical simulations for an idealized setup involving an ideal voltage-source load. Here, we provide several extensions with regard to both theory and application. First, we propose an alternative to an acausal derivative term that was a part of the feedback strategy in [29]. Furthermore, we generalize the load model from an ideal voltage source to a more realistic RC load behind a Thévenin resistance. Patently, the most significant contribution over [29] is experimental validation of the proposed control strategy on a hardware testbed comprising five identical 48 V-to-12 V buck converters rated at 120 W switching at 20 kHz. Experimental results demonstrate spontaneous convergence to the interleaved state through a variety of large-signal disturbances including startup from arbitrary initial conditions, load steps, and converter addition. While the analysis considers an ideal, symmetric, and uniform setting with equal dc-bus voltages and equal values for filter elements, the exhaustive experimental validation establishes robustness of the control strategy to parasitics, and parametric and input variations that are inescapable in any hardware implementation.

The remainder of this paper is organized as follows. Section II develops a model for the system of buck converters. Building upon that, we establish the nature and stability of solutions in Section III. We validate our analysis using a hardware prototype that implements our controller for parallel-connected buck converters in Section IV. Finally, we conclude in Section V by providing a few key directions for future work.

II. System Description and Modeling

In this section, we describe the model of the oscillator-controlled dc–dc buck converters that are connected in parallel and are supplying a common load. Using circuit laws and dynamics of the oscillators, we derive a coupled-oscillator model and then transform it to polar coordinates to extract phase information of the PWM waveforms.

A. Controller Description

The system architecture is illustrated in Fig. 2. It is composed of N parallel dc–dc buck converters indexed in the set $\mathcal{N}$

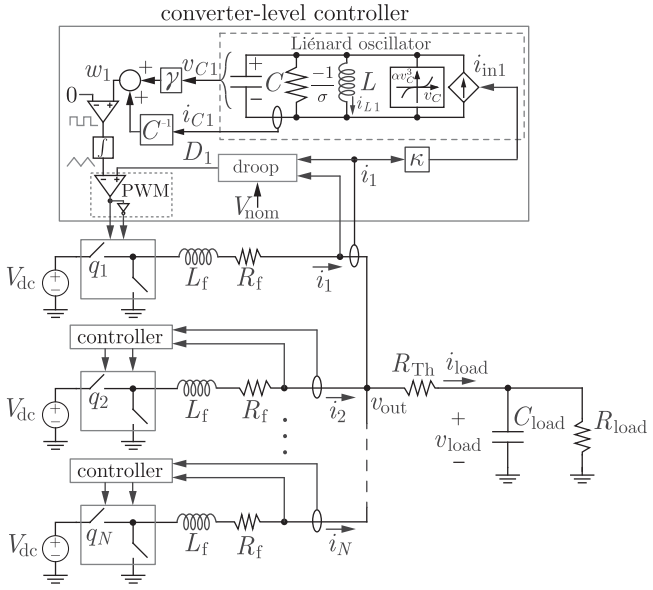

Fig. 2. System of parallel-connected buck converters with local controllers. The proposed controller has the dynamics of a nonlinear Liénard-type oscillator circuit, which takes the converter output current as feedback and generates the triangular PWM carrier at each converter by using a linear combination of its states. Droop control ensures decentralized power sharing.

supplying a common load. The controller for each converter (labeled *converter-level controller* for the first converter and simply as *controller* for the others) is decentralized and composed of two parts: 1) a discretized version of the second-order differential equation corresponding to the Liénard-type oscillators (labeled as *Liénard oscillator* for the first converter) that is responsible for switch interleaving; and 2) a slower-timescale droop-control-based voltage-regulation method (labeled as *droop* for the first converter).

The virtual-oscillator inductor and capacitor, L and C, are selected such that the oscillator resonant frequency coincides with the switching frequency $\omega_{\rm sw} = 1/\sqrt{LC}$ (the switching period is denoted by $T_{\rm sw} = 2\pi/\omega_{\rm sw}$). Furthermore, ensuring that $\sqrt{L/C} \ll 1$ renders the jth oscillator voltage $v_{Cj}(t)$ to be nearly sinusoidal [18]. The oscillator further consists of a negative conductance $-\sigma$ and a voltage-dependent current source αv_{Cj}^3, where $\alpha \in \mathbb{R}$ is a positive real constant. Next, the jth comparator and integrator act on a scaled sum of $v_{Cj}(t)$ and $i_{Cj}(t)$ to yield the PWM carrier (the comparator creates a square wave and the integrator produces the carrier). Finally, the switch pulses are generated in a typical fashion, where the carrier and duty ratio D_j are fed to a comparator and associated logic. This proposed structure for carrier generation is independent of the controller that governs the duty ratio. The outer-loop controller that generates the duty ratio runs on a much slower time scale. Here, we consider a prototypical droop controller that yields the duty ratio for each converter (details are in Section II-C). Each converter has an inductive output filter $L_{\rm f}$ (with parasitic resistance $R_{\rm f}$) and dc input voltage $V_{\rm dc}$. The load is modeled as a parallel combination of a resistor $R_{\rm load}$ and a capacitor $C_{\rm load}$ behind a Thévenin resistance $R_{\rm Th}$.

B. Parallel-converter System Model in Polar Coordinates

To analyze interleaving, it is necessary to describe the evolution of the phases corresponding to the switching signals of the converters controlled as shown in Fig. 2. Kirchhoff's laws yield the following dynamics for the inductor current i_{Lj} and capacitor voltage v_{Cj} for the jth oscillator in each controller:

$$L\frac{di_{Lj}}{dt} = v_{Cj}, \quad C\frac{dv_{Cj}}{dt} = (\sigma v_{Cj} - \alpha v_{Cj}^3) - i_{Lj} + i_{{\rm in}j}. \tag{1}$$

Here, $i_{{\rm in}j}$ denotes the input current that serves as feedback to the oscillator (see Fig. 2). Defining $\varepsilon := \sqrt{L/C}$, $x_j := \varepsilon i_{Lj}$, and $y_j := v_{Cj}$, the above dynamics can be rewritten as

$$\dot{x}_j = \omega_{\rm sw} y_j, \quad \dot{y}_j = -\omega_{\rm sw} x_j + \varepsilon\omega_{\rm sw}\left(\sigma y_j - \alpha y_j^3\right) + \varepsilon\omega_{\rm sw} i_{{\rm in}j}. \tag{2}$$

Note that x_j and y_j are orthogonal. To extract the phase dynamics, we define the amplitude and instantaneous phase angle corresponding to (2) as follows:

$$r_j := \sqrt{x_j^2 + y_j^2}, \quad \phi_j := \arctan\left(\frac{x_j}{y_j}\right). \tag{3}$$

To simplify analysis, we will focus on the phase-angle offset $\theta_j = \phi_j - \omega_{\rm sw} t$, which quantifies the angle difference with respect to a nominal reference frame rotating at the switching frequency $\omega_{\rm sw}$. Algebraic and trigonometric manipulations applied to (2) yield the following amplitude and phase-offset dynamics:

$$\begin{aligned}\dot{r}_j &= \varepsilon\omega_{\rm sw}\sigma r_j \cos^2(\omega_{\rm sw}t + \theta_j) - \varepsilon\omega_{\rm sw}\alpha r_j^3 \cos^4(\omega_{\rm sw}t + \theta_j) \\ &\quad + \varepsilon\omega_{\rm sw} i_{{\rm in}j}\cos(\omega_{\rm sw}t + \theta_j), \\ \dot{\theta}_j &= -\frac{\varepsilon\omega_{\rm sw}}{2}\left(\sigma - \alpha r_j^2\cos^2(\omega_{\rm sw}t + \theta_j)\right)\sin(2\omega_{\rm sw}t + 2\theta_j) \\ &\quad - \frac{\varepsilon\omega_{\rm sw}}{r_j} i_{{\rm in}j}\sin(\omega_{\rm sw}t + \theta_j).\end{aligned} \tag{4}$$

Given that (4) is time varying, it is difficult to analyze. We average it over one switch cycle to obtain the following averaged model:[1]

$$\begin{aligned}\dot{\overline{r}}_j &= \frac{\varepsilon\omega_{\rm sw}}{2}\left(\sigma\overline{r}_j - 3\alpha\overline{r}_j^3\right) + \frac{\varepsilon\omega_{\rm sw}^2}{2\pi}\int_{t=0}^{T_{\rm sw}} i_{{\rm in}j}\cos(\omega_{\rm sw}t + \overline{\theta}_j)dt \\ \dot{\overline{\theta}}_j &= -\frac{\varepsilon\omega_{\rm sw}^2}{2\pi\overline{r}_j}\int_{t=0}^{T_{\rm sw}} i_{{\rm in}j}\sin(\omega_{\rm sw}t + \overline{\theta}_j)dt\end{aligned} \tag{5}$$

where $\overline{r}_j$ and $\overline{\theta}_j$ are the averaged states. The derivation of (5) uses integration by parts and ignores second-order (i.e., $\mathcal{O}(\varepsilon^2)$) terms (see [21] for details on a similar proof for a different application). Furthermore, it can be shown that in the parametric regime $\varepsilon \ll 1$, where waveforms are sinusoidal, the original oscillator dynamics can be approximated by the averaged model with $\mathcal{O}(\varepsilon)$ error [21], [30], [31].

[1]For a time-varying dynamical system $\dot{x} = \varepsilon f(x,t,\varepsilon)$, where vector field $f(x,t,\varepsilon)$ is time periodic with period $T > 0$ (i.e., $f(x,t,\varepsilon) = f(x,t+T,\varepsilon)$), and $0 < \varepsilon \ll 1$, the associated *time-averaged dynamical system* is given by $\dot{\overline{x}} = \varepsilon\overline{f}(\overline{x}) = \varepsilon\frac{1}{T}\int_{\tau=0}^{T} f(\overline{x},\tau,0)d\tau$. The solution of the averaged system is $\mathcal{O}(\varepsilon)$ *close* to the solution of the original system, i.e., $||x(t,\varepsilon) - \overline{x}(\varepsilon t)||_2 = \mathcal{O}(\varepsilon) \quad \forall t \in [0, t^*]$, for some $t^* > 0$ for which unique solutions exist for both systems and assuming $||x(0,\varepsilon) - \overline{x}(0)||_2 = \mathcal{O}(\varepsilon)$ [30].

C. Feedback and Coupled-oscillator Dynamical Model

The feedback for the oscillators is through the current $i_{\mathrm{in}j}$, which, as shown in Fig. 2, is constructed as follows:

$$i_{\mathrm{in}j} = \kappa i_j \tag{6}$$

where $\kappa > 0$ is a feedback gain and i_j is the output current of the buck converter. Furthermore, the signal used to generate the PWM carrier wave, w_j, is built as the following linear combination of the virtual-oscillator dynamic states:

$$w_j = \frac{1}{C} i_{Cj} + \gamma v_{Cj} \tag{7}$$

where

$$\gamma := \frac{R_{\mathrm{f}}}{L_{\mathrm{f}}}. \tag{8}$$

It turns out that the above strategy is equivalent to constructing the feedback as

$$i_{\mathrm{in}j} = \kappa \left(\gamma i_j + \frac{di_j}{dt} \right) \tag{9}$$

with the PWM carrier wave picked to be the virtual-capacitor voltage and the coefficient of nonlinearity for the voltage-dependent current source in the oscillator accordingly rescaled as follows:

$$w_j = v_{Cj}, \quad \alpha' = \frac{\alpha}{\sqrt{\omega_{\mathrm{sw}}^2 + \gamma^2}}. \tag{10}$$

For subsequent developments, we transition to work in this equivalent system for analytical convenience, since the feedback in (9) brings forth the coupling between the oscillators [see (51)]. However, while the feedback and PWM carrier wave generation through (9) and (10) facilitate analysis, they involve an acausal derivative term that challenges implementation. Therefore, the hardware implementation is built with the priorly introduced feedback and PWM carrier wave generation method in (6) and (7). We prove the equivalence of (6), (7) and (9), (10) in Appendix A.

The duty-ratio commands for the individual oscillators are generated using droop control. The droop relation for the jth buck converter yields the following voltage reference:

$$V_{\mathrm{ref}j} = V_{\mathrm{nom}} - m i_j \tag{11}$$

where $m > 0$ is the droop slope, and V_{nom} is the nominal output voltage. The buck converter achieves the target voltage ($V_{\mathrm{ref}j}$) through a proportional–integral regulator with a feedthrough term. In particular, the duty cycle is governed by

$$V_{\mathrm{dc}} D_j = k_p \left(V_{\mathrm{ref}j} - v_{\mathrm{out}} \right) + \int k_i \left(V_{\mathrm{ref}j} - v_{\mathrm{out}} \right) dt + V_{\mathrm{ref}j} \tag{12}$$

where k_p and k_i are the proportional and integral gains, respectively, and v_{out} is the output voltage (see Fig. 2). In typical implementations, k_p and k_i are picked so that the duty-ratio commands vary on a much slower timescale in comparison to the switching period [3].

A variety of other advanced outer-loop control techniques have been proposed in the literature to improve attributes such as transient response, current distribution, and output-voltage regulation [32], [33]. Along these lines, accurate current sharing is critical in multiphase architectures, since it can prevent inductor saturation and limit thermal stress [34]. With that being said, our approach to interleaving the switching waveforms is decoupled from—and hence agnostic to—outer-loop control strategies; in this work, we adopt the classical droop-control strategy discussed above without loss of generality.

With the feedback strategy adopted in (6) and (7), and droop control for generating the duty cycle shown in (12), it emerges that the dynamics in (5) boil down to the following:

$$\begin{aligned} \dot{\overline{r}}_j &= h_j(\overline{r}_j) \; - \varepsilon \omega_{\mathrm{sw}} R_{\mathrm{Th}} \sqrt{\xi^2 + \chi^2} \sum_{k=1}^{N} \zeta_k \cos(\overline{\theta}_{jk} + \delta) \\ \dot{\overline{\theta}}_j &= \frac{\varepsilon \omega_{\mathrm{sw}} R_{\mathrm{Th}} \sqrt{\xi^2 + \chi^2}}{\overline{r}_j} \sum_{k=1}^{N} \zeta_k \sin(\overline{\theta}_{jk} + \delta) \end{aligned} \tag{13}$$

where we define $\overline{\theta}_{jk} := \overline{\theta}_j - \overline{\theta}_k$, and

$$\zeta_j := \frac{V_{\mathrm{dc}} \sin(D_j \pi) \kappa}{\pi L_{\mathrm{f}}} \frac{L_{\mathrm{f}}^2}{(\omega_{\mathrm{sw}} L_{\mathrm{f}})^2 + R_{\mathrm{f}}^2} \tag{14}$$

$$h_j(\overline{r}_j) := \frac{\varepsilon \omega_{\mathrm{sw}}}{2} \left(\sigma \overline{r}_j - 3\alpha \overline{r}_j^3 + 2\zeta_j \right) \tag{15}$$

$$\xi := \frac{\psi_1 \left(1 + \eta\right)^{-1}}{\omega_{\mathrm{sw}} L_{\mathrm{f}} \left(1 - \psi_1 \left(1 + \eta\right)^{-1} \psi_2\right)} \tag{16}$$

$$\chi := \frac{\left(1 - \eta\right)^{-1}}{\omega_{\mathrm{sw}} L_{\mathrm{f}} \left(1 - \psi_1 \left(1 + \eta\right)^{-1} \psi_2\right)} \tag{17}$$

$$\delta := \sin^{-1} \left(\frac{\xi}{\sqrt{\xi^2 + \chi^2}} \right) \tag{18}$$

with η, ψ_1, and ψ_2 given by

$$\eta := \left(1 - \frac{1}{\omega_{\mathrm{sw}}^2 R_{\mathrm{load}} C_{\mathrm{load}}} \right)^{-1} \frac{N}{\omega_{\mathrm{sw}}^2 C_{\mathrm{load}} L_{\mathrm{f}}} \tag{19}$$

$$\psi_1 := \frac{R_{\mathrm{f}} + N R_{\mathrm{Th}}}{\omega_{\mathrm{sw}} L_{\mathrm{f}}} - \frac{\eta}{\omega_{\mathrm{sw}} R_{\mathrm{load}} C_{\mathrm{load}}} \tag{20}$$

$$\psi_2 := -\frac{R_{\mathrm{f}} + N R_{\mathrm{Th}} + N R_{\mathrm{load}}}{\omega_{\mathrm{sw}} L_{\mathrm{f}}} + \eta \omega_{\mathrm{sw}} R_{\mathrm{load}} C_{\mathrm{load}}. \tag{21}$$

The derivation of the model in (13) hinges on the equivalence between the feedback and PWM carrier wave construction in (6) and (7) to that in (9) and (10) as shown in Appendix A. Building on this, we use integration by parts and a suite of circuit-theoretic notions including Kirchhoff's voltage law to describe the network dynamics, dynamics of the load voltage, a Fourier-series representation of the switching signal, and the input–output behavior of the dc–dc buck converters to arrive at (13). A sketch of this derivation is provided in Appendix B.

III. Equilibria and Stability

In this section, we enumerate different equilibria that result from the collective dynamics in (13) and comment on the stability of each. To that end, we will first establish a dynamical

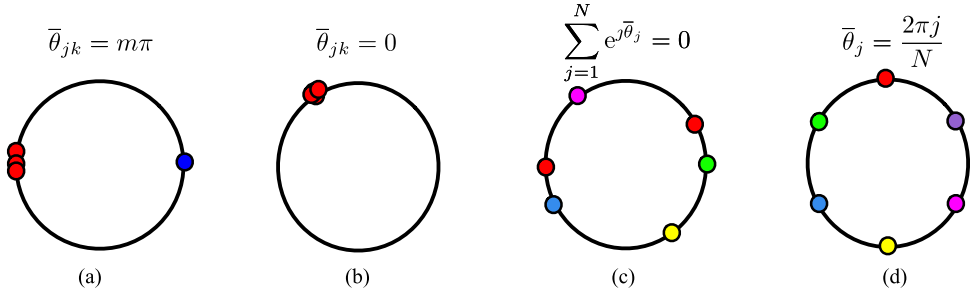

Fig. 3. Equilibria for the coupled oscillator dynamics (22). (a) Bi-cluster synchronous state. (b) Phase-synchronous state. (c) Generalized interleaved state. (d) Symmetric-interleaved state. Recall that $\overline{\theta}_j$ is the averaged phase-angle offset (with respect to a nominal reference frame rotating at the switching frequency) corresponding to the voltage of the virtual capacitor, v_{Cj} (and hence of its corresponding carrier waveform) for the jth oscillator. Furthermore, $\overline{\theta}_{jk} = \overline{\theta}_j - \overline{\theta}_k$.

model that collects and compactly represents all the individual oscillator dynamics in (13).

To evaluate stability of different equilibria, we make the assumption that $D_j = D_k \ \forall j,k \in \mathcal{N}$, which is true in the averaged sense and for time horizons pertinent to stability analysis of the interleaved state. From (14), we see that this implies $\zeta_j = \zeta_k =: \zeta \ \forall j,k \in \mathcal{N}$, which further renders $h_j(\overline{r}_j) =: h(\overline{r}_j), \forall j \in \mathcal{N}$. Furthermore, we also assume $\delta = 0$, which translates to an ideal setup where the Thévenin resistance on the load side is negligibly small and the switching frequency is high [see (18)]. With these assumptions in place, the dynamics in (13) can be compactly and collectively expressed as

$$\dot{\overline{r}} = H - \rho C 1_N \,, \quad \dot{\overline{\theta}} = \rho R^{-1} \, S 1_N \tag{22}$$

where $\overline{r} = [\overline{r}_1, \ldots, \overline{r}_N]^{\mathrm{T}}$, $\overline{\theta} = [\overline{\theta}_1, \ldots, \overline{\theta}_N]^{\mathrm{T}}$, and $H \in \mathbb{R}^N$, $N \times N$ real matrices R, C, S, and $\rho \in \mathbb{R}$ are given by

$$[H]_j = h(\overline{r}_j), \quad R = \mathrm{diag}\{\overline{r}\} \tag{23}$$

$$[C]_{j\ell} = \cos(\overline{\theta}_{jl}), \quad [S]_{j\ell} = \sin(\overline{\theta}_{jl}) \tag{24}$$

$$\rho = \varepsilon \omega_{\mathrm{sw}} R_{\mathrm{Th}} \zeta \sqrt{\xi^2 + \chi^2}. \tag{25}$$

To clarify the notation above, $[X]_{jk}$ represents the entry in the jth row and the kth column of matrix X; for vector x, $\mathrm{diag}\{x\}$ denotes the diagonal matrix obtained by stacking elements of x on the main diagonal, and 1_N denotes the length-N vector with all ones.

Note that the phase dynamics in (22) are not defined for $\overline{r}_j = 0$; indeed, the very notion of a radius is ill-posed when $\overline{r}_j \leq 0$. Hence, we first establish conditions such that the radii remain greater than zero. In particular, when the number of oscillators is upper bounded as follows:

$$N < \frac{1}{R_{\mathrm{Th}} \sqrt{\xi^2 + \chi^2}} \tag{26}$$

the set

$$\mathcal{I} := \left\{ (\overline{r}, \overline{\theta}) \in \mathbb{R}^N_{\geq 0} \times \mathbb{T}^N : \overline{r}_j > 0, \forall j \in \mathcal{N} \right\} \tag{27}$$

where $\mathbb{T}^N$ denotes the N-dimensional torus, is positively invariant with the designed feedback (6). To see this, consider that from the amplitude dynamics in (22), we obtain

$$\begin{aligned} \dot{\overline{r}}_j &= \varepsilon \omega_{\mathrm{sw}} \left(\frac{\sigma \overline{r}_j - \alpha \overline{r}_j^3}{2} + \zeta - R_{\mathrm{Th}} \sqrt{\xi^2 + \chi^2} \sum_{k=1}^{N} \zeta \cos(\overline{\theta}_{jk}) \right) \\ &\geq \frac{\varepsilon \omega_{\mathrm{sw}}}{2} \left(\sigma \overline{r}_j - \alpha \overline{r}_j^3 \right) + \varepsilon \omega_{\mathrm{sw}} \zeta \left(1 - N R_{\mathrm{Th}} \sqrt{\xi^2 + \chi^2} \right). \end{aligned} \tag{28}$$

So, if (26) holds, then

$$\dot{\overline{r}}_j \geq \frac{\varepsilon \omega_{\mathrm{sw}}}{2} \left(\sigma \overline{r}_j - \alpha \overline{r}_j^3 \right) + r_\circ \tag{29}$$

where $r_\circ$ is a positive constant. Clearly, $\forall \ \overline{r}_j < \sqrt{\sigma/\alpha}, \dot{\overline{r}}_j > 0$, which renders $\mathcal{I}$ to be positively invariant.

From the above discussion, we can conclude that R has all positive entries. At equilibrium, where $\dot{\overline{\theta}} = 0_N$ (0_N denotes the length-N vector with all zeros), we have from (22) that

$$S 1_N = 0_N. \tag{30}$$

Given the definition of matrix S in (24), one can identify different types of equilibria that satisfy the constraint in (30) (sketched on the phase plane in Fig. 3): a) bi-cluster synchronous state, b) phase-synchronous state, c) generalized interleaved state, and d) symmetric-interleaved state: the desired state where the phases of the PWM carriers are uniformly spaced apart. We formally define and study these next, and in each case, we *validate* that the phases indeed satisfy the constraint for equilibria, namely (30). We also comment on the *stability* of each.

A. Bi-cluster Synchronous State

The coupled system is said to be in the bi-cluster synchronous state if the phases evolve as

$$\overline{\theta}_j - \overline{\theta}_k = m\pi \quad \forall j,k \in \mathcal{N}, \forall m \in \mathbb{Z}. \tag{31}$$

The bi-cluster synchronous state is illustrated in Fig. 3(a).

Validity: To see that this is indeed an equilibrium, note from (24) that $[S]_{j\ell} = \sin(\overline{\theta}_{jl}) = 0, \forall j,k \in \mathcal{N}$ when $\overline{\theta}_j - \overline{\theta}_k = m\pi, \forall m \in \mathbb{Z}$. This further implies that phases defined by (31) satisfy $S 1_N = 0_N$, and hence, the bi-cluster synchronous state is an equilibrium of the dynamics (22).

Stability: Using linearization-based arguments, we show that this bi-cluster synchronous state is locally unstable unless the number of oscillators in the two clusters is equal. To establish

this, consider that the Jacobian of the linearized version of (22) around equilibria $\overline{\theta}_j - \overline{\theta}_k = m\pi$, where $m \in \mathbb{Z}$, has the following block-diagonal form:

$$J = \left[\begin{array}{c|c} J_{\rm A} & 0_{N\times N} \\ \hline 0_{N\times N} & J_{\rm D} \end{array}\right] \tag{32}$$

where $0_{N\times N}$ is the $N \times N$ matrix with all entries equal to 0. The entries of $J_{\rm A}$ and $J_{\rm D}$ are specified as

$$[J_{\rm A}]_{j\ell} = \begin{cases} h'(\overline{r}_j^*), & \text{if } j = \ell \\ 0, & \text{if } j \neq l \end{cases}$$

$$[J_{\rm D}]_{j\ell} = \begin{cases} -\frac{\rho}{\overline{r}_j^*}, & \text{if } j \neq l,\ \overline{\theta}_{j\ell} = 2m\pi \\ \frac{\rho}{\overline{r}_j^*}, & \text{if } j \neq l,\ \overline{\theta}_{j\ell} = (2m+1)\pi \\ -\sum_{\ell=1,\ell\neq j}^{N} [J_{\rm D}]_{j\ell}, & \text{if } j = \ell, \end{cases}$$

where $m \in \mathbb{Z}$ and $\overline{r}_j^*$ is the equilibrium radius for the jth oscillator. Since J is block diagonal, its eigenvalues are those of $J_{\rm A}$ and $J_{\rm D}$. In the following, we focus the analysis on the eigenvalues of $J_{\rm D}$. Since $\overline{\theta}_j - \overline{\theta}_k = m\pi$, the phases of the oscillators belong to one of the two clusters on the circle (depending on whether m is odd or even). Two cases need attention:

1) *The sizes of the two clusters differ by more than one:* Denote e_j to be the length-N unit basis vector with 1 at the jth entry and zeros elsewhere. Denote ℓ to be the index of any node in the bigger cluster. The diagonal entries of $J_{\rm D}$ corresponding to oscillators in the bigger cluster are positive, and since $e_\ell^{\rm T} J_{\rm D} e_\ell > 0$, it is not negative semidefinite; therefore, $J_{\rm D}$ must have at least one positive eigenvalue [35].
2) *The sizes of the clusters differ by one:* The diagonal entries are either 0 (for the nodes in the bigger cluster) or -2 (for the nodes in the smaller cluster). Thus, there exists a symmetric principal minor of order 2 (corresponding to two nodes in distinct clusters) of the form

$$\frac{\rho}{2} \cdot \begin{bmatrix} 0 & \pm 1 \\ \pm 1 & -2 \end{bmatrix}$$

which features a positive eigenvalue. Therefore, $J_{\rm D}$ cannot be negative semidefinite [35] in this case as well.

In conclusion, $J_{\rm D}$ (and hence, J) has at least one eigenvalue with positive real part. This establishes the local instability of clusters, where the phase equilibria satisfy $\overline{\theta}_j - \overline{\theta}_k = m\pi$, and the number of oscillators in each cluster is not the same.

B. Phase-synchronous State

This corresponds to the state where the phases of all oscillators are perfectly synchronized:

$$\overline{\theta}_j = \overline{\theta}_k \quad \forall j, k \in \mathcal{N}. \tag{33}$$

This state is illustrated in Fig. 3(b). Note that it is recovered as a special case from the bi-cluster synchronous state for $m = 0$.

Validity: To see that this is indeed an equilibrium, note from (24) that $[S]_{j\ell} = \sin(\overline{\theta}_{jl}) = 0$, $\forall j, k \in \mathcal{N}$ when $\overline{\theta}_j = \overline{\theta}_k$. This further implies that phases defined by (33) satisfy $S1_N = 0_N$, and hence, the phase-synchronous state is indeed an equilibrium of the dynamics (22).

Stability: Note that the phase-synchronous state is recovered from the bi-cluster synchronous state when $m = 0$. Therefore, the stability result from Section III-A applies in this case as well. In particular, for the case $m = 0$, $J_{\rm D}$ in (33) is a Laplacian matrix of a complete graph and, therefore, is positive semidefinite. This establishes that the phase-synchronous state is locally unstable.

C. Generalized Interleaved State

This is a generalized notion of the symmetric-interleaved state and captures the setting where the phases of the oscillators evolve functionally constrained as follows:

$$\sum_{j=1}^{N} \mathrm{e}^{\jmath\overline{\theta}_j} = 0 \tag{34}$$

where $\jmath = \sqrt{-1}$. This state is also known as the phase-balanced state, and it is widely studied in the coupled-oscillator literature [36]. Closer to the application at hand, it was investigated for an asymmetric interleaving application [7], where the first harmonic was eliminated to minimize the current ripple. The generalized interleaved state is illustrated in Fig. 3(c).

Validity: Unlike the bi-cluster synchronous state and the phase-synchronized state, in this case, S is not a null matrix, and therefore, condition (30) is not satisfied trivially. Nonetheless, it turns out that when S is not a null matrix, then $S1_N = 0_N$ if and only if $C1_N = 0_N$ (see [27, Proposition 2]). For the generalized interleaved state where $\sum_{j=1}^{N} \mathrm{e}^{\jmath\overline{\theta}_j} = 0$, it is true that $C1_N = 0_N$ *and* $S1_N = 0_N$, and therefore, this indeed corresponds to an equilibrium of the phase dynamics in (22).

Stability: We construct a directed graph to establish the nature of equilibria in the oscillator dynamics (22). Let N nodes of the graph denote the oscillators, and if the vector field governing $\dot{\overline{\theta}}_j$ has a $\overline{\theta}_{jk}$ term (i.e., the evolution of the jth oscillator dynamics depends on the dynamics of the kth oscillator), then there is an edge between nodes j and k. The phase dynamics in (22) can be compactly recast as follows:

$$\dot{\overline{\theta}} = R^{-1} B \sin(B^{\rm T}\overline{\theta}) \tag{35}$$

where $B \in \mathbb{R}^{N\times\binom{N}{2}}$ is the edge-oriented incidence matrix of the underlying complete graph. Furthermore, with regard to notation, for $\theta = [\theta_1, \ldots, \theta_N]^{\rm T} \in \mathbb{T}^N$, $\sin(\theta) := [\sin(\theta_1), \ldots, \sin(\theta_N)]^{\rm T}$ and $\cos(\theta) := [\cos(\theta_1), \ldots, \cos(\theta_N)]^{\rm T}$.

We introduce a coordinate change to $\widetilde{\theta} = B^{\rm T}\overline{\theta} \in \mathbb{R}^{\binom{N}{2}}$, which captures angle differences between the oscillators. In this new set of coordinates, the phase dynamics can be written as

$$\dot{\widetilde{\theta}} = \rho B^{\rm T} R^{-1} B \sin\widetilde{\theta}\,. \tag{36}$$

Consider the following potential function:

$$V(\overline{r}, \widetilde{\theta}) = -\sum_{j=1}^{N} \int_{s=0}^{\overline{r}_j} h(s)ds + 1_N^{\rm T} RB\cos\widetilde{\theta} \tag{37}$$

from which, it follows that

$$\dot{V}(\overline{r}, \widetilde{\theta}) = -\left(H - \rho B\cos\widetilde{\theta}\right)^2 - \rho(\sin\widetilde{\theta})^{\rm T} B^{\rm T} R R^{-1} B \sin\widetilde{\theta}.$$

Note that $\dot{V}(\overline{r},\widetilde{\theta}) \leq 0$, since it is the sum of two quadratic terms with a negative leading sign. Thus, the sublevel sets of V are compact (closed due to continuity and bounded as $V(\overline{r},\widetilde{\theta})$ is radially unbounded).

Finally, by LaSalle's invariance principle [30], all trajectories starting in $\mathcal{I}$ [defined in (27)] converge to the subset identified by $\dot{V}=0$, i.e., amplitudes and phases are such that $B\sin\widetilde{\theta}=0_N$ (which is true if and only if $S1_N=0_N$, which implies $C1_N=0$ when S is not a null matrix) and $H-\rho C1_N=0$ (which gives $H=0_N$ when S is not a null matrix). As discussed earlier, $S1_N=0_N$ gives rise to either the bi-cluster synchronous state (of which the phase-synchronous state is a special case) or the generalized interleaved state. We have already established that the bi-cluster synchronous state is locally unstable. Therefore, almost all trajectories must eventually converge to the generalized interleaved state.

D. Symmetric-interleaved State

The multiphase system is said to be in a symmetric-interleaved state if the phases of the coupled oscillators evolve uniformly spaced apart as follows:

$$\overline{\theta}_j = j\frac{2\pi}{N} + \theta_\circ \pmod{2\pi} \quad \forall j \in \mathcal{N}, \quad 0 \leq \theta_\circ \leq 2\pi. \tag{38}$$

The symmetric-interleaved state is illustrated in Fig. 3(d).

Validity: We established previously that the generalized interleaved state [where phases are governed by (34)] is indeed an equilibrium of the phase dynamics (22). Notice that the symmetric-interleaved state, where phases are governed by (38), is a special case of the generalized interleaved state and, therefore, satisfies the condition (30) as well.

Stability: To establish whether the interleaved state is locally stable, we begin by shifting the amplitude and phase dynamics from (22) to the origin as follows:

$$\mu_j = \overline{r}_j - \overline{r}^*, \quad \varphi_j = \overline{\theta}_j - j\frac{2\pi}{N} \tag{39}$$

where $\overline{r}^*$ denotes the equilibrium radius, which solves $h(\overline{r}^*)=0$. Now, the dynamics of the coupled system (22) around this equilibrium can be written as

$$\begin{aligned}\dot{\mu}_j &= h(\overline{r}^*+\mu_j) \; - \rho\sum_{k=1}^{N}\cos\left(\frac{2\pi(j-k)}{N}+\varphi_{jk}\right)\\ \dot{\varphi}_j &= \frac{\rho}{\overline{r}^*+\mu_j}\sum_{k=1}^{N}\sin\left(\frac{2\pi(j-k)}{N}+\varphi_{jk}\right)\end{aligned} \tag{40}$$

where $\varphi_{jk} := \varphi_j - \varphi_k$. We focus on the phase dynamics and leverage the fact that μ_j and φ_{jk} are small quantities as we are interested in the behavior around the neighborhood of the interleaved state, and therefore, $\sin\varphi_{jk} \approx \varphi_{jk}$, $\cos\varphi_{jk} \approx 1$ and $(\overline{r}^*+\mu_j)^{-1} \approx \frac{1}{\overline{r}^*}(1-\frac{\mu_j}{\overline{r}^*})$. With these simplifications in place and ignoring second-order terms like $\mu_j\varphi_{jk}$, the phase dynamics reduce to

$$\dot{\varphi} = \frac{\rho}{\overline{r}^*}J\varphi \tag{41}$$

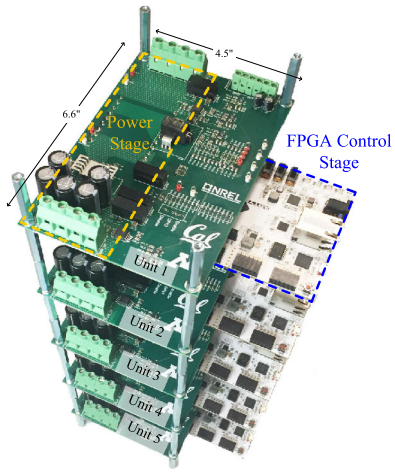

Fig. 4. Photograph of the experimental prototype: five dc–dc converters and associated controller boards. Note that there is no communication between controllers.

where $\varphi := [\varphi_1,\ldots,\varphi_N]^{\mathrm{T}} \in \mathbb{T}^N$ and J is a symmetric circulant matrix with entries given by

$$[J]_{j\ell} = \begin{cases} -1 & \text{if } j=\ell \\ -\cos\left(\frac{2\pi}{N}(j-\ell)\right), & \text{if } j\neq\ell. \end{cases}$$

Since J is a circulant matrix, its eigenvalues are given by

$$\lambda_j(J) = \sum_{k=0}^{N-1}\cos\left(\frac{2\pi k}{N}\right)\Omega_j^k \tag{42}$$

where $\Omega_j = \mathrm{e}^{\jmath 2\pi j/N}$ denotes one of the Nth roots of unity. Note that two of these eigenvalues are $-N/2$ and the rest are zero. Thus, the linearized phase dynamics around the symmetrically interleaved equilibrium are marginally stable.

IV. Experimental Validation

The proposed approach is validated with a hardware prototype of parallel-connected dc–dc buck converters with independent field-programmable gate array controllers, as shown in Fig. 4. The prototype consists of five independent converters rated at 120 W each, stepping down from 48 to 12 V at 20 kHz. The parameters for the controllers along with specifications and ratings of the prototype are listed in Table I. In this section, we first outline the design procedure that was followed to select the oscillator (controller) and converter parameters, following which we provide experimental results.

A. System Parameters and Controller Design

In this section, we discuss the rationale for the design choices listed in Table I. The oscillator parameters L and C are tuned to the switching frequency, i.e., $1/\sqrt{LC}=\omega_{\mathrm{sw}}=2\pi\times 20\times 10^3$ rad/s, while maintaining the quasi-harmonic regime, i.e., $\sqrt{L/C}=\varepsilon\ll 1$. We chose $\varepsilon=0.19$ in our implementation. Setting $\sigma>0$ satisfies the Liénard condition for sustaining oscillations [16], and $\alpha=2\sigma/3$ yields a sinusoidal oscillation of unit amplitude for the oscillators, which aids in

TABLE I
SPECIFICATIONS, PARAMETERS, AND RATINGS FOR THE EXPERIMENTAL PROTOTYPE

Power Stage Hardware	48 V to 12 V step-down, 120 W per converter
L_{f}	141.6 μH $\pm 10\%$
R_{f}	13.70 mΩ
C_{load}	1100 μF $\pm 20\%$
R_{Th}	0.1 Ω $\pm 5\%$
R_{load}	1.6 Ω $\pm 10\%$
R_{par}	50 mΩ $\pm 5\%$
Switching frequency	20 kHz
MOSFET	Fairchild FDB035N10A
Gate driver	Silicon Labs SI8234
Current sensors	Allegro ACS730KLCTR
Voltage sensors	Broadcom ACPL-C87AT
Control Stage Hardware	
Device	Xilinx Artix-7 XC7A35T-L1CSG324I FPGA
Controller time step	150 ns
ADC sampling rate	500 kHz

Oscillator parameters	
σ	$90\,\Omega^{-1}$
α	$60\,\mathrm{A/V^3}$
L	$0.61\,\mu$H
C	$16.67\,\mu$F
Droop controller parameters	
k_p	$0.32\,\mathrm{V/V}$
k_i	$0.06\,\mathrm{s}^{-1}$
m	$1.5\,\mathrm{V/A}$
V_{nom}	$12\,\mathrm{V}$

regularizing the design. The current gain $\kappa > 0$ is necessary for interleaving and is chosen to be 10. (Empirically, we observe that very small values of κ result in slow convergence to the equilibrium state, while very large values of κ induce nonsinusoidal oscillator states with no convergence guarantees.) The droop controller gains k_p and k_i are selected so that the time constant of the controller is about 5 s, and there is a clear time-scale separation from the switching period. Furthermore, for each individual buck converter, L_{f} was selected to guarantee the continuous conduction mode at the selected operating point, and C_{load} is just sufficiently large to establish a constant voltage at the load side. Finally, we also verify that the sufficient positive invariance condition (26) derived in Section III is met so that phase dynamics are well-posed, i.e., $NR_{\mathrm{Th}}\sqrt{\xi^2+\chi^2} < 1$. Notice that in the ideal setup as $R_{\mathrm{Th}} \to 0$, the condition is always satisfied for all N. The current setup with the chosen physical parameters satisfies this condition up to 41 units.

Tolerances of various components utilized in the hardware setup are also listed alongside nominal values in Table I. While the analysis presumed an ideal and symmetric setup, the experimental results provided subsequently establish the robustness of the approach to a variety of parametric variations (including the ones in Table I that are readily quantifiable through values from datasheets).

We conducted four experimental tests to validate the performance and robustness of the proposed interleaving control method: 1) startup of five units from arbitrary initial conditions; 2) addition of one unit to four units in the steady state; 3) a load step applied to five units in the steady state; and 4) unit addition to a nonsymmetric network with lossy lines.

The setup and experiments listed above are sketched in Fig. 5. Next, we provide results from these experiments and demonstrate that, in each case, the proposed controller ensures interleaving in the steady state without any communication between converters.

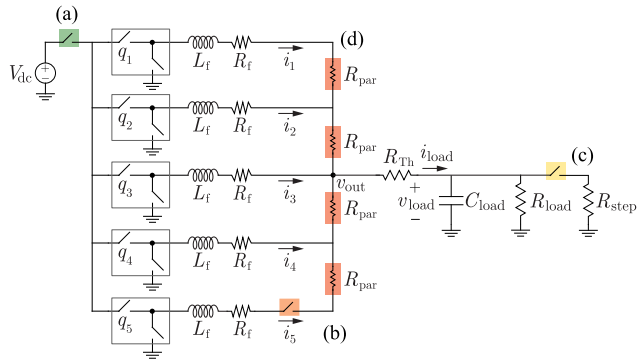

Fig. 5. Circuit diagram illustrating experiments performed. (a) Startup from arbitrary initial conditions. (b) Addition of one converter to system. (c) Load step. (d) Unit addition in a nonsymmetric network with parasitics (in this case, converters continue to sense local output voltages for droop control even though this is not explicitly depicted in the figure).

B. Startup From Arbitrary Initial Conditions

First, we consider the startup scenario in which five units are initiated simultaneously, each with arbitrary initial conditions. The dynamics of the load current and the ac components of the phase currents for this case are shown in Fig. 6. The phase currents i_j of the individual converters at the turn-on instant are arbitrarily spaced, which results in a larger ripple in i_{load}. After approximately 40 ms, the phase currents of the five converters settle to the interleaved state with $72^\circ = 360^\circ/5$ phase offset, and the ripple in i_{load} is visibly reduced.

C. Unit Addition

Next, to demonstrate the plug-and-play nature of the proposed control strategy, we investigate system performance when an additional converter is added. As shown in Fig. 7, the system is initialized in the steady state with four parallel units with phase currents that are $90^\circ = 360^\circ/4$ out of phase with adjacent units.

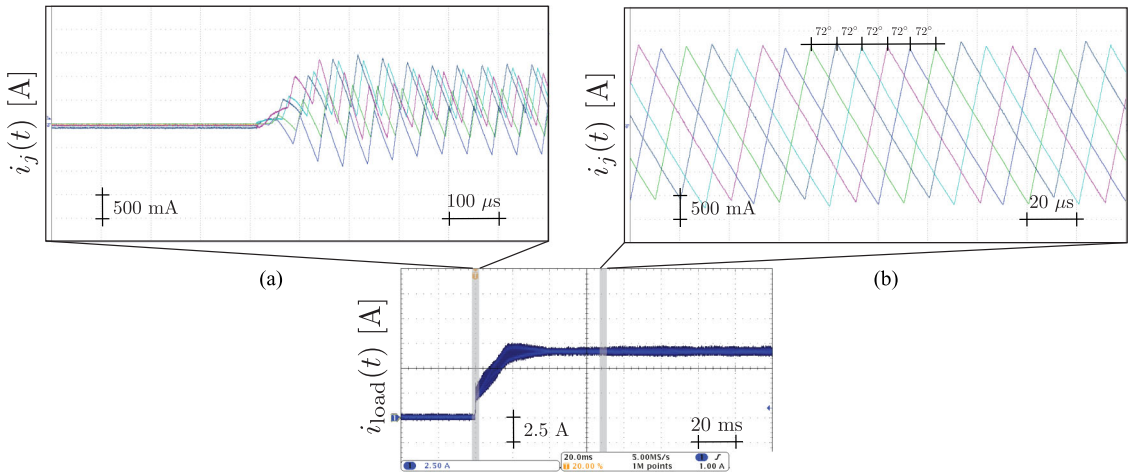

Fig. 6. (a) Five buck converters are started from arbitrary initial conditions with the designed oscillator-based controllers. (b) System achieves symmetric interleaving with 72° = 360°/5 phase spacing, and the droop controller maintains balanced currents in each of the five units in steady state.

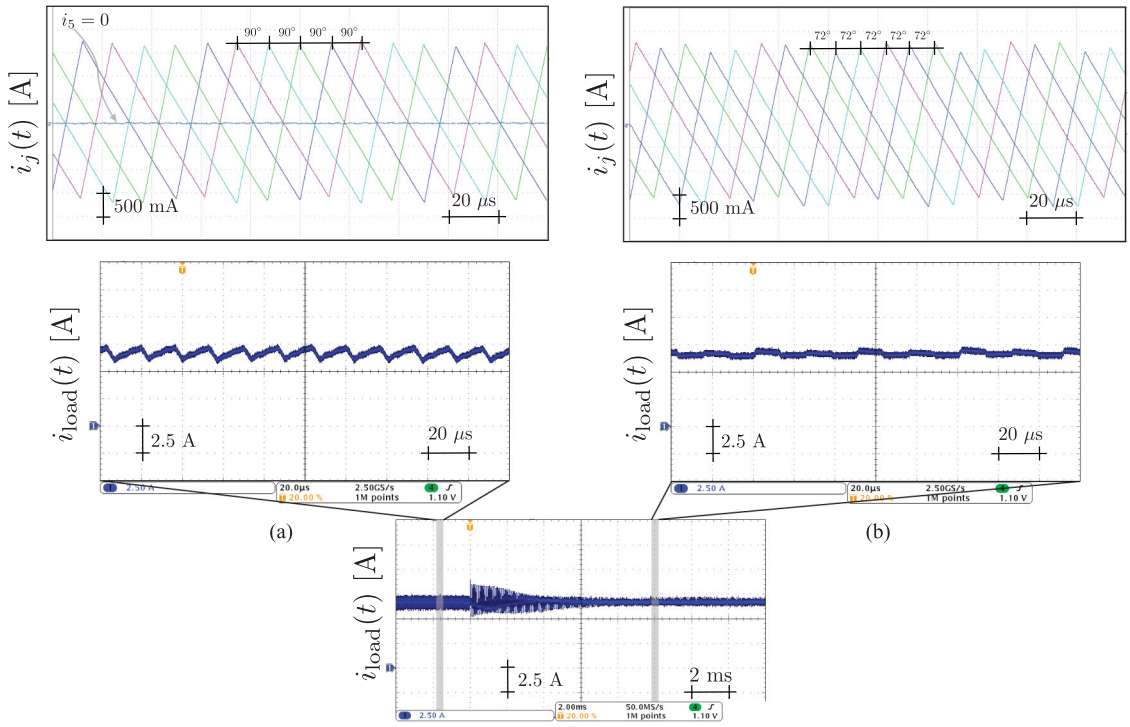

Fig. 7. One additional buck converter unit is added to four functioning units. The phase currents i_j automatically transition from having (a) 90° = 360°/4 phase shift to (b) 72° = 360°/5 phase shift.

After adding an additional fifth unit, the system reaches the interleaved state in approximately 6 ms with each phase current now 72° (360°/5) out of phase with adjacent units. The benefits of interleaving with additional units are also evident in reducing the load-current ripple. Again, the droop controller successfully maintains current sharing before and after the addition of the fifth unit.

D. Load Step

We experimentally implemented a load step to validate the robustness of the control method to typical operating transients. As shown in Fig. 8, the load is changed from $R_{\text{load}} = 1.6\ \Omega$ to $R_{\text{load}} = 1.3\ \Omega$ at $t = 0$ with five units connected. The system maintains the interleaved state before and after the transient, as indicated by the unchanged ripple magnitude in i_{load} and the unchanged 72° phase shift in phase currents i_j.

E. Nonideal Output Parallel Configuration

Finally, in order to validate the robustness of the proposed method to nonidealities in the parallel output configuration, we implemented the circuit shown in Fig. 5, where deliberately introduced resistors R_{par} induce a nontrivial output impedance to each converter. This eliminates the ideal parallel connection

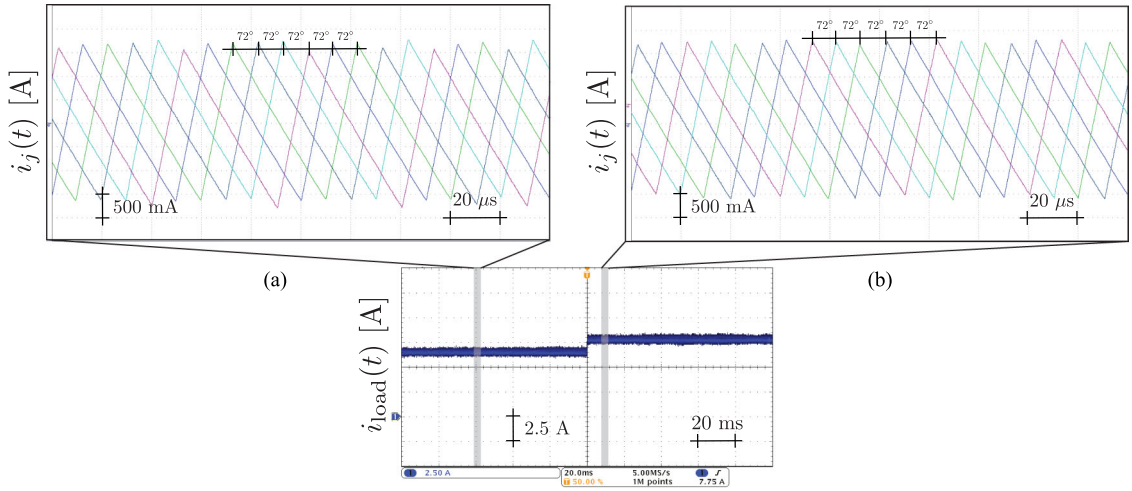

Fig. 8. To evaluate robustness to load variations, a load step from (a) $R_{\text{load}} = 1.6\ \Omega$ to (b) $R_{\text{load}} = 1.3\ \Omega$ at $t = 0$ is introduced with five units in steady state. The convergence to the new steady state is almost instantaneous, and the system maintains the symmetric-interleaved state with $72^\circ = 360^\circ/5$ phase spacing between converters.

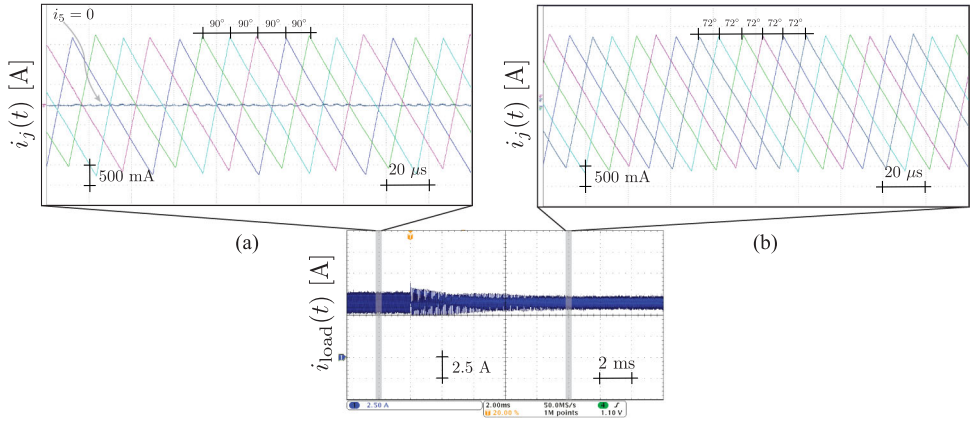

Fig. 9. Addition of one unit to four units in steady state with the nonsymmetric setup and lossy network shown in Fig. 5. The phase currents i_j automatically transition from having (a) $90^\circ (360^\circ/4)$ phase shift to (b) $72^\circ (360^\circ/5)$ phase shift.

between the dc–dc converters. With this circuit, we executed the task of adding one unit to four units in steady state. As shown in Fig. 9, four units are initially interleaved with $90^\circ = 360^\circ/4$ degree phase shift in currents. When the fifth unit is added, the system reaches the new interleaved state after approximately 8 ms, at which point the phase shifts automatically adjust to $72^\circ = 360^\circ/5$. Note from the figure that the ripple in the load current reduces with the additional unit. The presence of the nonidealities does increase the ripple (compared to the case shown in Fig. 7) by approximately 50%. Regardless, this experiment demonstrates the robustness of the method to achieve interleaving even in the presence of modestly large nonidealities in the output loading configuration. Moreover, these nonidealities have a minimal impact on the droop controller and its ability to ensure current sharing between the units.

V. Conclusion and Directions for Future Work

In this paper, we proposed a decentralized control strategy to achieve interleaving in a system of parallel-connected buck converters. Our approach utilized a nonlinear-oscillator-based controller that processes a local current measurement to generate the PWM carrier waveform. It offers enhanced reliability and flexibility compared to existing algorithms for modular architectures that are at best distributed in nature since there is no need for external communication. A system of parallel-connected buck converters with droop control was built as a hardware prototype, and we experimentally demonstrated the efficacy of the proposed control algorithm for modular plug-and-play operation as well as robustness to load variations. Extending the analysis to other dc–dc converter topologies and network architectures is the focus of ongoing investigations.

Appendix A
Equivalence of (6) and (7) to (9) and (10)

Figure 10(a) illustrates the closed-loop system as described by the system of equations (6) and (7): we refer to this as "system (a)" subsequently. The capacitor voltages of the oscillators, collected in the vector y, are used to generate signals in w, which dictate the switching in the buck converters. This is done using the linear time-invariant filter $s + \gamma$ (see (7) in Section II-C).

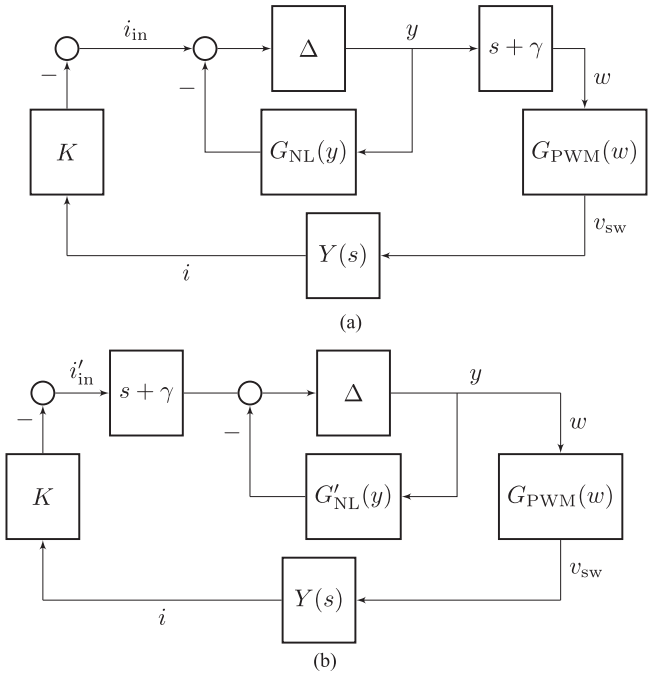

Fig. 10. Block-diagram representations of the interconnected system with the equivalent coupled oscillator model dynamics (13). (a) Version that is implemented in hardware. (b) Equivalent version leveraged for analysis.

Furthermore, $\Delta = G_{\text{L}}(s)I_N$ captures the linear component of the nonlinear-oscillator dynamics, with $G_{\text{L}}(s)$ given by

$$G_{\text{L}}(s) := \frac{\varepsilon s}{s^2 - \varepsilon\sigma s + \omega_{\text{sw}}^2}. \tag{43}$$

The oscillator dynamics are obtained by placing this in feedback with the cubic nonlinearity αy_j^3 (1). The approach to decompose the dynamics of Liénard-type oscillators into linear and nonlinear subsystems is commonly used for analysis, since it permits the application of describing-function approaches that extend frequency-domain methods to nonlinear systems [37]. In this particular case, the describing function for the feedback static nonlinearity, αy_j^3, is denoted by $G_{\text{NL}}(y_j)$. All of these are collected in $G_{\text{NL}}(y) = \text{diag}\{G_{\text{NL}}(y_1), \ldots, G_{\text{NL}}(y_N)\}$. Finally, w feeds into a signum function with windowed integrators, a droop controller that generates the requisite duty command for power sharing, and a comparator with a carrier wave that generates the switching signals $q(t)$, which when multiplied by the dc-input voltage V_{dc} gives the switched voltages, $v_{\text{sw}} = \text{diag}\{V_{\text{dc}}q_1, \ldots, V_{\text{dc}}q_N\}$. These dynamics described above are captured in the frequency domain via the scalar transfer function block $s+\gamma$ and the describing function $G_{\text{PWM}}(w)$. Note that $G_{\text{PWM}}(w)$ has a similar decoupled structure like $G_{\text{NL}}(y)$, and it collects the individual describing functions on the diagonal, i.e., $G_{\text{PWM}}(w) = \text{diag}\{G_{\text{PWM}}(w_1), \ldots, G_{\text{PWM}}(w_N)\}$. To close the loop, the feedback (function of the inductor currents, i, in the buck converters) is described by Kirchhoff's current laws, captured by the admittance of the electrical network, denoted by $Y(s)$, and matrix $K = \kappa I_N$, which is a diagonal static transfer function that incorporates the current gains [see (6)].

Figure 10(b) shows the block diagram of the equivalent system (from an input–output standpoint), described by the system of equations (9) and (10): we refer to this as "system (b)" subsequently. Notice that it differs from the original system in Fig. 10(a) in two aspects: 1) the placement of the filter block $s+\gamma$, which now filters the feedback currents instead of the output voltages and 2) the describing function for the nonlinearity, denoted by $G'_{\text{NL}}(y)$. This is due to the fact that the systems have different coefficients α and α' for their nonlinearities. Next, we will derive the relationship between α and α' to ensure that the input–output behavior of the systems is the same.

Observe that the i_j to w_j relation in system (a) is given by

$$\frac{\kappa G_{\text{L}}(s) i_j(s)}{(s+\gamma)} = \left(1 + G_{\text{L}}(s)\,(s+\gamma)\,G_{\text{NL}}\left(\frac{w_j(s)}{(s+\gamma)}\right)\right) w_j(s) \tag{44}$$

and, similarly, the i_j to w_j relation in the equivalent system (b) is described by

$$\kappa G_{\text{L}}(s)(s+\gamma) i_j(s) = \left(1 + G_{\text{L}}(s) G'_{\text{NL}}\left(w_j\right)\right) w_j(s)\,. \tag{45}$$

Since $G_{\text{L}}(s)$ is a linear block, it commutes with the scalar block $s+\gamma$. Thus, for the systems in (44) and (45) to be equivalent,

$$(s+\gamma) G_{\text{NL}}\left(\frac{w_j(s)}{(s+\gamma)}\right) = G'_{\text{NL}}(w_j(s)). \tag{46}$$

Since $\varepsilon \ll 1$ by design, $G_{\text{L}}(s)$ has bandpass characteristics with resonant frequency ω_{sw}. Therefore, we can assume $w_j = A\cos\omega_{\text{sw}}t$. Using the sinusoidal input describing function approach as outlined in [38] and [37], we have

$$G_{\text{NL}}(y_j) = \frac{3\alpha A^2}{4}\,, G'_{\text{NL}}(y_j) = \frac{3\alpha' A^2}{4}\,. \tag{47}$$

At $s = \jmath\omega_{\text{sw}}$,

$$\begin{aligned}(s+\gamma) G_{\text{NL}}\left(\frac{w_j(s)}{(s+\gamma)}\right) &= \frac{3\alpha A^2 (\jmath\omega_{\text{sw}} + \gamma)}{4(\omega_{\text{sw}}^2 + \gamma^2)} \mathrm{e}^{\tan^{-1}(-\gamma/\omega_{\text{sw}})} \\ &= \frac{3\alpha A^2}{4\sqrt{\omega_{\text{sw}}^2 + \gamma^2}}\,. \end{aligned} \tag{48}$$

Thus, for

$$\alpha' = \frac{\alpha}{\sqrt{\omega_{\text{sw}}^2 + \gamma^2}} \tag{49}$$

both the systems (a) and (b) have equivalent input–output behavior.

APPENDIX B
DERIVATION OF (13)

Denote the switching signal of the jth buck converter as $q_j(t) \in \{0, 1\}$. Kirchhoff's voltage law indicates that

$$V_{\rm dc} q_j(t) - R_{\rm f} i_j(t) - L_{\rm f} \frac{di_j}{dt} - R_{\rm Th} i_{\rm load} = v_{\rm load} \tag{50}$$

where $i_{\rm load} := \sum_{j=1}^{N} i_j$. Recognizing (9), we can write

$$i_{{\rm in}j} = \kappa \left(\frac{R_{\rm f}}{L_{\rm f}} i_j + \frac{di_j}{dt} \right) = \kappa \left(V_{\rm dc} q_j(t) - R_{\rm Th} i_{\rm load} - v_{\rm load} \right). \tag{51}$$

Substituting for $i_{{\rm in}j}$ from (51) into (5) yields

$$\begin{aligned} \dot{\overline{r}}_j = {} & \frac{\varepsilon \omega_{\rm sw}}{2} (\sigma \overline{r}_j - 3\alpha \overline{r}_j^3) - \int_{t=0}^{T_{\rm sw}} \frac{\varepsilon \omega_{\rm sw}^2 \kappa v_{\rm load}}{2\pi L_{\rm f}} \cos(\omega_{\rm sw} t + \overline{\theta}_j) dt \\ & + \frac{\varepsilon \omega_{\rm sw}^2 \kappa}{2\pi L_{\rm f}} \int_{t=0}^{T_{\rm sw}} V_{\rm dc} q_j(t) \cos(\omega_{\rm sw} t + \overline{\theta}_j) dt \\ & - \frac{\varepsilon \omega_{\rm sw}^2 R_{\rm Th} \kappa}{2\pi L_{\rm f}} \int_{t=0}^{T_{\rm sw}} i_{\rm load} \cos(\omega_{\rm sw} t + \overline{\theta}_j) dt \end{aligned} \tag{52}$$

$$\begin{aligned} \dot{\overline{\theta}}_j = {} & - \frac{\varepsilon \omega_{\rm sw}^2 \kappa}{2\pi \overline{r}_j L_{\rm f}} \int_{t=0}^{T_{\rm sw}} V_{\rm dc} q_j(t) \sin(\omega_{\rm sw} t + \overline{\theta}_j) dt \\ & + \frac{\varepsilon \omega_{\rm sw}^2 R_{\rm Th} \kappa}{2\pi \overline{r}_j L_{\rm f}} \int_{t=0}^{T_{\rm sw}} i_{\rm load} \sin(\omega_{\rm sw} t + \overline{\theta}_j) dt \\ & - \frac{\varepsilon \omega_{\rm sw}^2 \kappa}{2\pi L_{\rm f}} \int_{t=0}^{T_{\rm sw}} v_{\rm load} \sin(\omega_{\rm sw} t + \overline{\theta}_j) dt. \end{aligned} \tag{53}$$

The PWM switching signal, $q_j(t)$, can be written as the following series for a particular duty ratio D_j [39]:

$$q_j(t) = D_j + \sum_{m=1}^{\infty} \frac{2}{m\pi} \sin(D_j m\pi) \cos(m(\omega_{\rm sw} t + \theta_j)). \tag{54}$$

Substituting for $q_j(t)$ from (54) into (52) yields

$$\begin{aligned} \dot{\overline{r}}_j = {} & \frac{\varepsilon \omega_{\rm sw}}{2} \left(\sigma \overline{r}_j - 3\alpha \overline{r}_j^3 \right) - \frac{\varepsilon \omega_{\rm sw}^2 \kappa}{2\pi L_{\rm f}} \int_{t=0}^{T_{\rm sw}} v_{\rm load} \sin(\omega_{\rm sw} t + \overline{\theta}_j) dt \\ & + \frac{\varepsilon \omega_{\rm sw}^2 R_{\rm Th} \kappa}{2\pi \overline{r}_j L_{\rm f}} \int_{t=0}^{T_{\rm sw}} i_{\rm load} \sin(\omega_{\rm sw} t + \overline{\theta}_j) dt + \frac{\varepsilon \omega_{\rm sw}^2 \kappa V_{\rm dc}}{2\pi L_{\rm f}} \\ & \times \sum_{m=1}^{\infty} \int_{t=0}^{T_{\rm sw}} \frac{2 \sin D_j m\pi}{m\pi} \cos(m(\omega_{\rm sw} t + \theta_j)) \cos(\omega_{\rm sw} t + \overline{\theta}_j) dt \end{aligned} \tag{55}$$

$$\begin{aligned} = {} & \frac{\varepsilon \omega_{\rm sw}}{2} \left(\sigma \overline{r}_j - 3\alpha \overline{r}_j^3 \right) + \frac{\varepsilon \omega_{\rm sw}^2 \kappa V_{\rm dc} \sin(D_j \pi)}{\pi L_{\rm f}} \\ & + \frac{\varepsilon \omega_{\rm sw}^2 R_{\rm Th} \kappa}{2\pi \overline{r}_j L_{\rm f}} \int_{t=0}^{T_{\rm sw}} i_{\rm load} \sin(\omega_{\rm sw} t + \overline{\theta}_j) dt \\ & - \frac{\varepsilon \omega_{\rm sw}^2 \kappa}{2\pi L_{\rm f}} \int_{t=0}^{T_{\rm sw}} v_{\rm load} \sin(\omega_{\rm sw} t + \overline{\theta}_j) dt. \end{aligned} \tag{56}$$

In simplifying the second integral on the first line of (56), we have leveraged the following: 1) $\overline{\theta}_j(t)$ is $\mathcal{O}(\varepsilon)$ close to $\theta_j(t)$ and 2) since integrals of sines and cosines evaluate to zero over their period, only the fundamental harmonic remains in the $q_j(t)$ expansion and the average of $\cos^2(\omega_{\rm sw} t + \overline{\theta}_j)$ over its time period is $1/2$. Similarly, we get the following for the phase dynamics:

$$\begin{aligned} \dot{\overline{\theta}}_j = {} & \frac{\varepsilon \omega_{\rm sw}^2 R_{\rm Th} \kappa}{2\pi \overline{r}_j L_{\rm f}} \int_{t=0}^{T_{\rm sw}} i_{\rm load} \sin(\omega_{\rm sw} t + \overline{\theta}_j) dt \\ & - \frac{\varepsilon \omega_{\rm sw}^2 \kappa}{2\pi L_{\rm f}} \int_{t=0}^{T_{\rm sw}} v_{\rm load} \sin(\omega_{\rm sw} t + \overline{\theta}_j) dt. \end{aligned} \tag{57}$$

Finally, note that the load current and voltage, $i_{\rm load}$ and $v_{\rm load}$, are governed by the following dynamics:

$$L_{\rm f} \frac{di_{\rm load}}{dt} + (R_{\rm f} + N R_{\rm Th}) i_{\rm load} = \sum_{j=1}^{N} V_{\rm dc} q_j(t) - N v_{\rm load}. \tag{58}$$

$$C_{\rm load} \frac{dv_{\rm load}}{dt} + \frac{v_{\rm load}}{R_{\rm load}} = i_{\rm load}. \tag{59}$$

While (59) follows straightforwardly from the circuit laws for an RC tank, (58) is derived by summing up all N instances of (50). Going back to (56) and (57), we use integration by parts for integrals involving $i_{\rm load}$ and $v_{\rm load}$, where we substitute appropriately from (58) and (59) to compute the requisite derivatives. Algebraic simplifications then yield (13).

REFERENCES

[1] D. J. Perreault and J. G. Kassakian, "Distributed interleaving of paralleled power converters," *IEEE Trans. Circuits Syst. I, Fundam, Theory Appl.*, vol. 44, no. 8, pp. 728–734, Aug. 1997.

[2] W. Huang and B. Lehman, "A compact coupled inductor for interleaved multiphase dc–dc converters," *IEEE Trans. Power Electron.*, vol. 31, no. 10, pp. 6770–6775, Oct. 2016.

[3] J. M. Guerrero, J. C. Vasquez, J. Matas, L. G. De Vicuña, and M. Castilla, "Hierarchical control of droop-controlled AC and DC microgrids: A general approach toward standardization," *IEEE Trans. Ind. Electron.*, vol. 58, no. 1, pp. 158–172, Jan. 2011.

[4] M. Schuck and R. C. Pilawa-Podgurski, "Ripple minimization in asymmetric multiphase interleaved dc-dc switching converters," in *Proc. IEEE Energy Convers. Congr. Expo.*, Sep. 2013, pp. 133–139.

[5] M. Schuck and R. C. Pilawa-Podgurski, "Current ripple cancellation for asymmetric multiphase interleaved dc-dc switching converters," in *Proc. IEEE Power Energy Conf. Illinois*, 2013, pp. 162–168.

[6] M. Schuck and R. C. Pilawa-Podgurski, "Input current ripple reduction through interleaving in single-supply multiple-output dc-dc converters," in *Proc. 14th IEEE Workshop Control Model. Power Electron.*, 2013, pp. 1–5.

[7] M. Schuck, A. D. Ho, and R. C. Pilawa-Podgurski, "Asymmetric interleaving in low-voltage CMOS power management with multiple supply rails," *IEEE Trans. Power Electron.*, vol. 32, no. 1, pp. 715–722, Jan. 2017.

[8] M. Schuck and R. C. Pilawa-Podgurski, "Ripple minimization through harmonic elimination in asymmetric interleaved multiphase dc–dc converters," *IEEE Trans. Power Electron.*, vol. 30, no. 12, pp. 7202–7214, Dec. 2015.

[9] L. Che and M. Shahidehpour, "DC microgrids: Economic operation and enhancement of resilience by hierarchical control," *IEEE Trans. Smart Grid*, vol. 5, no. 5, pp. 2517–2526, Sep. 2014.

[10] M. Baranwal, S. M. Salapaka, and M. V. Salapaka, "Robust decentralized voltage control of dc-dc converters with applications to power sharing and ripple sharing," in *Proc. Amer. Control Conf.*, Jul. 2016, pp. 7444–7449.

[11] A. Costabeber, P. Mattavelli, and S. Saggini, "Digital time-optimal phase shedding in multiphase buck converters," *IEEE Trans. Power Electron.*, vol. 25, no. 9, pp. 2242–2247, Sep. 2010.

[12] Y. C. Wang and Y. Y. Tzou, "Design and realization of a digital multiphase-interleaved VRM controller using FPGA," in *Proc. 33rd Annu. Conf. IEEE Ind. Electron. Soc.*, Nov. 2007, pp. 1978–1982.

[13] E. A. Burton *et al.*, "FIVR—Fully integrated voltage regulators on 4th generation Intel Core SoCs," in *Proc. IEEE Appl. Power Electron. Conf. Expo.*, Mar. 2014, pp. 432–439.
[14] Y. C. Chen, J. D. Hsu, Y. A. Ang, and T. Y. Yang, "A new phase shedding scheme for improved transient behavior of interleaved boost pfc converters," in *Proc. IEEE Appl. Power Electron. Conf. Expo.*, Mar. 2014, pp. 1916–1919.
[15] J. W. Kolar, G. R. Kamath, N. Mohan, and F. C. Zach, "Self-adjusting input current ripple cancellation of coupled parallel connected hysteresis-controlled boost power factor correctors," in *Proc. IEEE Power Electron. Spec. Conf.*, Jun. 1995, vol. 1, pp. 164–173.
[16] S. H. Strogatz, *Nonlinear Dynamics and Chaos: With Applications to Physics, Biology, Chemistry, and Engineering*. Boulder, CO, USA: Westview Press, 2014.
[17] M. Colombino, D. Groß, and F. Dörfler, "Global phase and voltage synchronization for power inverters: A decentralized consensus-inspired approach," in *Proc. 56th IEEE Conf. Decis. Control*, 2017, pp. 5690–5695.
[18] B. B. Johnson, S. V. Dhople, A. O. Hamadeh, and P. T. Krein, "Synchronization of parallel single-phase inverters with virtual oscillator control," *IEEE Trans. Power Electron.*, vol. 29, no. 11, pp. 6124–6138, Nov. 2014.
[19] L. A. B. Tôrres, J. P. Hespanha, and J. Moehlis, "Power supplies dynamical synchronization without communication," in *Proc. IEEE Power Energy Soc. Gen. Meeting*, Jul. 2012, pp. 1–6.
[20] L. A. B. Tôrres, J. P. Hespanha, and J. Moehlis, "Synchronization of identical oscillators coupled through a symmetric network with dynamics: A constructive approach with applications to parallel operation of inverters," *IEEE Trans. Autom. Control*, vol. 60, no. 12, pp. 3226–3241, Dec. 2015.
[21] M. Sinha, F. Dörfler, B. B. Johnson, and S. V. Dhople, "Uncovering droop control laws embedded within the nonlinear dynamics of Van der Pol oscillators," *IEEE Trans. Control Netw. Syst.*, vol. 4, no. 2, pp. 347–358, Jun. 2017.
[22] M. Li, Y. Gui, J. M. Guerrero, R. Teodorescu, and J. C. Vasquez, "Adaptive synchronization of grid-connected three-phase inverters by using virtual oscillator control," in *Proc. IEEE Appl. Power Electron. Conf. Expo.*, Mar. 2018, pp. 1130–1135.
[23] J. Hu and H. Ma, "Synchronization of the carrier wave of parallel three-phase inverters with virtual oscillator control," *IEEE Trans. Power Electron.*, vol. 32, no. 10, pp. 7998–8007, Oct. 2017.
[24] C. De Persis and B. Jayawardhana, "On the internal model principle in the coordination of nonlinear systems," *IEEE Trans. Control Netw. Syst.*, vol. 1, no. 3, pp. 272–282, Sep. 2014.
[25] G.-B. Stan and R. Sepulchre, "Analysis of interconnected oscillators by dissipativity theory," *IEEE Trans. Autom. Control*, vol. 52, no. 2, pp. 256–270, Feb. 2007.
[26] R. Sepulchre, D. Paley, and N. Leonard, "Collective motion and oscillator synchronization," in *Cooperative Control*. New York, NY, USA: Springer, 2005, pp. 189–205.
[27] M. Sinha, F. Dörfler, B. B. Johnson, and S. V. Dhople, "Phase balancing in globally connected networks of Liénard-type oscillators," in *Proc. 56th IEEE Conf. Decis. Control*, Dec. 2017, pp. 595–600.
[28] M. Sinha, F. Dörfler, B. B. Johnson, and S. V. Dhople, "Synchronization of Liénard-type oscillators in heterogeneous electrical networks," in *Proc. 4th Indian Control Conf.*, Dec. 2017, pp. 240–245.
[29] M. Sinha, S. Dhople, B. Johnson, M. Rodriguez, and J. Poon, "Decentralized interleaving of paralleled dc-dc buck converters," in *Proc. IEEE 18th Workshop Control Model. Power Electron.*, Jul. 2017, pp. 1–6.
[30] H. Khalil, *Nonlinear Systems*, 3rd ed. Upper Saddle River, NJ, USA: Prentice-Hall, 2002.
[31] S. E. Tuna, "Synchronization analysis of coupled Liénard-type oscillators by averaging," *Automatica*, vol. 48, no. 8, pp. 1885–1891, 2012.
[32] Y. Panov and M. M. Jovanovic, "Stability and dynamic performance of current-sharing control for paralleled voltage regulator modules," *IEEE Trans. Power Electron.*, vol. 17, no. 2, pp. 172–179, Mar. 2002.
[33] H. Wang, M. Han, R. Han, J. M. Guerrero, and J. C. Vasquez, "A decentralized current-sharing controller endows fast transient response to parallel dc-dc converters," *IEEE Trans. Power Electron.*, vol. 33, no. 5, pp. 4362–4372, May 2018.
[34] H. Mao, L. Yao, C. Wang, and I. Batarseh, "Analysis of inductor current sharing in nonisolated and isolated multiphase dc-dc converters," *IEEE Trans. Ind. Electron.*, vol. 54, no. 6, pp. 3379–3388, Dec. 2007.
[35] R. A. Horn and C. R. Johnson, *Matrix Analysis*. Cambridge, U.K.: Cambridge Univ. Press, 2012.
[36] F. Dörfler and F. Bullo, "Synchronization in complex oscillator networks: A survey," *Automatica*, vol. 50, no. 6, pp. 1539–1564, 2014.
[37] S. Sastry, *Nonlinear Systems: Analysis, Stability, and Control*, vol. 10. New York, NY, USA: Springer, 2013.
[38] W. E. Vander Velde, *Multiple-Input Describing Functions and Nonlinear System Design*. New York, NY, USA: McGraw-Hill, 1968.
[39] J. Sun, "Pulse-width modulation," in *Dynamics and Control of Switched Electronic Systems*. New York, NY, USA: Springer, 2012, pp. 25–61.

Mohit Sinha (S'13) received the B.Tech. degree in electrical engineering from the Indian Institute of Technology, Delhi, New Delhi, India, in 2011. He is currently working toward the Ph.D. degree in electrical engineering with the University of Minnesota, Minneapolis, MN, USA.

He was an Engineer with National Power Thermal Power Corporation from 2011 to 2013. He has held research and development positions with Siemens Corporate Technology, National Renewable Energy Laboratory, and Suzlon Energy Limited. His research interests include control and modeling of power electronics, nonlinear system analysis, and networked dynamical systems.

Mr. Sinha was a recipient of the Electrical Engineering Department Fellowship in 2013.

Jason Poon (S'11) received the B.S. degree from the Olin College of Engineering, Needham, MA, USA, in 2012, and the M.S. degree from the University of California, Berkeley, CA, USA, in 2015, both in electrical engineering. He is currently working toward the Ph.D. degree with the Department of Electrical Engineering and Computer Sciences, University of California, Berkeley.

He has held R&D positions with Dialog Semiconductor, the National Renewable Energy Laboratory, the Massachusetts Institute of Technology, ABB Corporate Research, and the National University of Singapore. His research interests include power electronics circuits and systems with applications in renewable energy, electrified transportation, miniaturized and on-chip power, wireless power transfer, and energy infrastructure and distribution.

Mr. Poon is a recipient of the National Science Foundation Graduate Research Fellowship, the National Defense Science and Engineering Graduate Fellowship, and a Best Paper Award at the 2016 IEEE Workshop on Control and Modeling for Power Electronics for his work on distributed fault-tolerant power electronics.

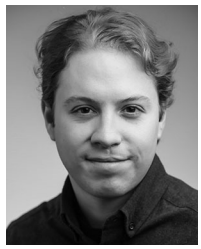

Brian B. Johnson (S'08–M'13) received the M.S. and Ph.D. degrees in electrical and computer engineering from the University of Illinois at Urbana–Champaign, Urbana, IL, USA, in 2010 and 2013, respectively.

He is currently an Assistant Professor with the Department of Electrical and Computer Engineering, University of Washington, Seattle, WA, USA. Prior to joining the University of Washington in 2018, he was an Engineer with the National Renewable Energy Laboratory, Golden, CO, USA. His research interests include renewable energy systems, power electronics, and control systems.

Dr. Johnson was a recipient of the National Science Foundation Graduate Research Fellowship in 2010. He is an Associate Editor for the IEEE TRANSACTIONS ON ENERGY CONVERSION.

Miguel Rodriguez (S'06–M'11) was born in Gijon, Spain, in 1982. He received the M.S. and Ph.D. degrees in telecommunication engineering from the University of Oviedo, Oviedo, Spain, in 2006 and 2011, respectively.

From 2011 to 2013, he was a Postdoctoral Research Associate with the Colorado Power Electronics Center, University of Colorado, Boulder, CO, USA. In 2013, he joined Advanced Micro Devices, Inc., Fort Collins, CO, as a member of the Low Power Advanced Development Group. His current research interests include dc–dc conversion and digital control, analysis of power delivery networks, and linear and switched integrated voltage regulators for microprocessors and systems on a chip.

Sairaj V. Dhople (M'13) received the B.S., M.S., and Ph.D. degrees in electrical engineering from the University of Illinois at Urbana–Champaign, Urbana, IL, USA, in 2007, 2009, and 2012, respectively.

He is currently an Assistant Professor with the Department of Electrical and Computer Engineering, University of Minnesota, Minneapolis, MN, USA, where he is with the Power and Energy Systems research group. His research interests include modeling, analysis, and control of power electronics and power systems with a focus on renewable integration.

Dr. Dhople received the National Science Foundation CAREER Award in 2015. He is an Associate Editor for the IEEE TRANSACTIONS ON ENERGY CONVERSION and the IEEE TRANSACTIONS ON POWER SYSTEMS.